The Mechanisms Responsible for Large Near-Surface Vertical Vorticity within Simulated Supercells and Quasi-Linear Storms

Christian H. Boyer*† and Johannes M. L. Dahl

Atmospheric Science Group, Department of Geosciences, Texas Tech University, Lubbock, Texas

*Corresponding author: Christian H. Boyer, boyer1c@cmich.edu

†Current Affiliation: Department of Earth and Atmospheric Sciences, Central Michigan University, Mount Pleasant, Michigan

Early Online Release: This preliminary version has been accepted for publication in *Monthly Weather Review*, may be fully cited, and has been assigned DOI 10.1175/MWR-D-20-0082.1. The final typeset copyedited article will replace the EOR at the above DOI when it is published.

ABSTRACT

Despite their structural differences, supercells and quasi-linear convective systems (QLCS) are both capable of producing severe weather, including tornadoes. Previous research has highlighted multiple potential mechanisms by which horizontal vorticity may be reoriented into the vertical at low levels, but it is not clear in which situation what mechanism dominates. In this study, we use the CM1 model to simulate three different storm modes, each of which developed relatively large near-surface vertical vorticity. Using forward-integrated parcel trajectories, we analyze vorticity budgets and demonstrate that there seems to be a common mechanism for maintaining the near-surface vortices across storm structures. The parcels do not acquire vertical vorticity until they reach the base of the vortices. The vertical vorticity results from vigorous upward tilting and simultaneous vertical stretching. While the parcels analyzed in our simulations do have a history of descent, they do not acquire appreciable vertical vorticity during their descent. Rather, during the analysis period relatively large horizontal vorticity develops as a result of horizontal stretching by the horizontal wind, such that it can be effectively tilted into the vertical.

Accepted for publication in *Monthly Weather Review*. DOI 10.1175/MWR-D-20-0082.1.

1. Introduction

The development of near-surface rotation has been investigated for many years in both supercells and quasi-linear convective systems (QLCSs). There have been many different proposed mechanisms of acquiring positive vertical vorticity in the lowest tens of meters by reorienting the horizontal vorticity into the vertical (e.g., Davies-Jones and Brooks 1993; Davies-Jones 2000; Dahl et al. 2014; Markowski and Richardson 2014; Parker and Dahl 2015; Rotunno et al. 2017; Flournoy and Coniglio 2019; Roberts et al. 2020). These mechanisms generally fall into three categories (i) upward vortex line tilting via the downdraft (Davies-Jones and Brooks 1993; Markowski et al. 2008; Dahl et al. 2014; Dahl 2015; Parker and Dahl 2015), (ii) upward vortex line tilting via the updraft (Schenkman et al. 2012; Mashiko 2016; Roberts et al. 2016; Roberts and Xue 2017; Rotunno et al. 2017; Flournoy and Coniglio 2019), and (iii) downward vortex line tilting via the downdraft (Weisman and Trapp 2003; Trapp and Weisman 2003; Parker 2012; Dahl 2015).

The upward vortex line tilting via the downdraft mechanism was first proposed by Davies-Jones and Brooks (1993) and is often referred to as the DJB mechanism. This mechanism has been shown both in theoretical models (Davies-Jones 2000, 2017) and in numerical simulations (Davies-Jones and Brooks 1993; Dahl et al. 2014; Markowski and Richardson 2014; Parker and Dahl 2015). Fig. 1a depicts the process of tilting as well as the interaction of an initially horizontal vorticity vector with a downdraft. Horizontal vorticity is continually generated throughout the process, causing the vorticity vector to attain less downward inclination than the streamlines. As the streamlines turn horizontally near the ground, the vorticity vector is thus tilted into the vertical, leading to a vertical vorticity component as the streamline reaches its nadir very close to the surface.

In contrast to this mechanism, Rotunno et al. (2017) discussed the possibility of the updraft being the agent that facilitates the upward tilting of horizontal vorticity to achieve near-surface (lowest

Accepted for publication in *Monthly Weather Review*. DOI 10.1175/MWR-D-20-0082.1.

tens of meters) vertical vorticity. Through a parcel trajectory analysis in a supercell simulation and theoretical arguments, they showed that near-surface vertical vorticity is not acquired until after the parcel reaches its nadir. Therefore, the parcel attains substantial vertical vorticity after it enters the rising motion of a strong low-level updraft, indicating the importance of the updraft in tilting and subsequent stretching of the near-surface horizontal vorticity. This mechanism is shown in Fig. 1b.

The third mechanism involving the depression of horizontal vortex lines was discussed by Trapp and Weisman (2003) for QLCSs and Dahl (2015) for supercells. In this mechanism, the convective scale downdraft tilts the horizontal vorticity downward to the surface. Trapp and Weisman (2003) observed in their numerical simulations that the mesovortices are generated behind the outflow boundary of the QLCS with the cyclonic mesovortex forming to the south and the anticyclonic mesovortex forming to the north (Fig. 1c).

All of these processes have been shown to be present within supercells (Markowski and Richardson 2014; Dahl et al. 2014; Schenkman et al. 2014) and linear storm modes (Atkins and St. Laurent 2009; Flournoy and Coniglio 2019), which raises the question in which situation what mechanism is most relevant. Inspection of the different results indicates that different authors tend to look at different altitudes when analyzing the vorticity as well as different stages of vortex development. Our goal is to clarify the mechanism that maintains relatively intense near-surface vortices across archetypal storm structures. A trajectory analysis including vorticity budget calculations is performed on a vortex within each simulation to diagnose the sources of the storm's near-surface vertical vorticity.

The rest of the paper is structured as follows. In section 2 we describe the methodology of simulations and the associated trajectory analyses while section 3 presents the results. A discussion is given in section 4, followed by conclusions in section 5.

Accepted for publication in *Monthly Weather Review*. DOI 10.1175/MWR-D-20-0082.1.

2. Methods

a. Model Configuration and Base-state

Using the Bryan Cloud model 1 (CM1, Bryan and Fritsch 2002) release 19, simulations of a supercell, a quasi-two-dimensional squall line and a three-dimensional QLCS were performed. For all simulations, the model domain is 150 km x 148.8 km x 20 km with a horizontal grid spacing of 200 m and a stretched vertical grid with spacing of 20 m at the lowest level and 300 m at the model top, resulting in 125 vertical levels. The lowest model level at which the u and v wind components are defined is 10 m above ground level. A large numerical time step of 2.0 s is employed.

The upper and lower boundary conditions are free slip while the horizontal boundary conditions are open. A fifth-order advection scheme is employed in both the horizontal and vertical dimensions for all scalar and velocity variables. The fifth-order scheme results in implicit diffusion occurring in the simulations. Each simulation also employs the Morrison double-moment microphysics scheme (Morrison et al. 2005; Dawson et al. 2010). Lastly, no radiative or surface fluxes were applied and the Coriolis parameter was set to zero.

A horizontally-homogeneous base-state is used for all simulations, given by the Weisman-Klemp analytic sounding, which has modest convective available potential energy (CAPE, 1830 J kg^{-1}). In order to simulate the different storm modes, the wind profile was altered between the simulations. The Weisman-Klemp quarter-circle hodograph was used for the supercell/QLCS simulation[1], while the more linear quasi-two-dimensional squall line was initialized using the wind profile introduced by Rotunno et al. (1988).

The supercell/QLCS simulation was initialized using three warm bubbles, spaced 30 km apart from each other, with a 5 K temperature perturbation. This distance allowed the storms to grow and

[1]The supercell and QLCS both occur within the same simulation. The supercell forms at the southern end of the ongoing, larger-scale QLCS.

Accepted for publication in *Monthly Weather Review*. DOI 10.1175/MWR-D-20-0082.1.

mature prior to merging together and growing upscale. In the quasi-two-dimensional squall line simulation, storms were initiated using a breaking-dam-style cold pool with a potential temperature perturbation of -6 K and a depth of 2500 m that spanned the entire south-north direction of the domain. The squall line simulation included random potential temperature perturbations in the model domain to allow for some 3D structure (including 3D turbulence) to develop.

b. Trajectory Analysis and Vorticity Budget Calculations

Near-surface vortices were selected based on their maturity and persistence. In the simulations, one vortex was analyzed in each of the supercell and squall line cases while 2 adjacent vortices were analyzed in the QLCS. The vortices within the supercell/QLCS simulation were required to meet a threshold vertical vorticity value of 0.1 s^{-1} at the lowest model level (10 m). The vortices chosen within the supercell and QLCS stood out due to their strength, size and persistence when compared to the other vortices, and they remained at 0.1 s^{-1} vertical vorticity for at least five minutes. In the squall line simulation, none of the vortices stood out, and all of them remained relatively weak (vertical vorticity less than 0.1 s^{-1}) and short-lived. We thus randomly selected a typical vortex for our analysis.

After identifying a vortex of interest within the simulations, forward trajectories were calculated on a restart simulation prior to peak vortex strength. The parcels were initialized so that they were included within both the outflow and inflow regions of the storms and were seeded every 200 m in the horizontal and every 100 m in the vertical, beginning at 30 m AGL. The parcel trajectories were integrated forward in time on every model time step (2.0 s). The release time and number of parcels varied with each simulation. The number and release times of the parcels are as follows: 2 000 000 parcels at 6900 s (approximately 5 minutes before vortexgenesis) for the supercell, 1 875 000 parcels at 3900 s (approximately 40 minutes before vortexgenesis) in the quasi-two-dimensional

Accepted for publication in *Monthly Weather Review*. DOI 10.1175/MWR-D-20-0082.1.

squall line, and 2 250 000 parcels (approximately 15 minutes before vortexgenesis) at 6000 s for the QLCS. Since the parcels originated within the cold pool, relatively long histories were analyzed for the squall line and QLCS to ensure that at least part of the descent of the parcels was captured.

Due to the amount of parcels released in each simulation, it is unreasonable to analyze data on every parcel because we are interested only in those parcels that enter the vortex, so several criteria were set. First, the general area containing the vortex was identified, so an east-west, north-south window was set for each of the three vortices that the parcels had to enter. Depending upon the vortex, the horizontal search area had a diameter between 2 to 3 km in each direction. In addition to the area criterion, a height threshold was also used. The parcels had to enter the vortex within the lowest 100 m of the simulation. The time windows were set for the individual vortices, and were chosen during the mature stage of the vortices' lifespan. Therefore, the parcels were entering the vortex while it was at peak strength. The final criterion considered for the parcels was the vertical vorticity. The individual parcel had to reach a threshold value of at least 0.01 s^{-1} vertical vorticity. From the above criteria, the simulations of the supercell, quasi-two-dimensional squall line, and QLCS yielded 75, 14, and 61 parcels, respectively. In summary, we identify those parcels that enter the very bottom of mature vortices.

Along the trajectories, the time-integrated, 3D vorticity forcing terms were calculated within CM1 at every large time step. These terms were used to calculate the evolution along the trajectories of the horizontal vorticity magnitude, as well as the vertical vorticity component. The equation for the horizontal vorticity magnitude is given by

$$|\boldsymbol{\omega}_h| = \sqrt{\boldsymbol{\omega}_h \cdot \boldsymbol{\omega}_h}, \tag{1}$$

from which it follows that

$$\frac{D|\boldsymbol{\omega}_h|}{Dt} = \frac{1}{|\boldsymbol{\omega}_h|}\left(\xi\frac{D\xi}{Dt} + \eta\frac{D\eta}{Dt}\right). \tag{2}$$

Accepted for publication in *Monthly Weather Review*. DOI 10.1175/MWR-D-20-0082.1.

Here,

$$\frac{D\xi}{Dt} = \underbrace{-\xi\left(\frac{\partial v}{\partial y}+\frac{\partial w}{\partial z}\right)}_{\text{A}} + \underbrace{\left(\zeta\frac{\partial u}{\partial z}+\eta\frac{\partial u}{\partial y}\right)}_{\text{B}} - \underbrace{\left(\frac{\partial \alpha}{\partial y}\frac{\partial p}{\partial z}-\frac{\partial \alpha}{\partial z}\frac{\partial p}{\partial y}\right)}_{\text{C}} + \underbrace{\left(\frac{\partial F_y}{\partial z}-\frac{\partial F_y}{\partial z}\right)}_{\text{D}} \tag{3}$$

$$\frac{D\eta}{Dt} = \underbrace{-\eta\left(\frac{\partial u}{\partial x}+\frac{\partial w}{\partial z}\right)}_{\text{A}} + \underbrace{\left(\xi\frac{\partial v}{\partial x}+\zeta\frac{\partial v}{\partial z}\right)}_{\text{B}} - \underbrace{\left(\frac{\partial \alpha}{\partial z}\frac{\partial p}{\partial x}-\frac{\partial \alpha}{\partial x}\frac{\partial p}{\partial z}\right)}_{\text{C}} + \underbrace{\left(\frac{\partial F_x}{\partial z}-\frac{\partial F_z}{\partial x}\right)}_{\text{D}}. \tag{4}$$

The vertical vorticity equation is given by

$$\frac{D\zeta}{Dt} = \underbrace{-\zeta\left(\frac{\partial u}{\partial x}+\frac{\partial v}{\partial y}\right)}_{\text{A}} + \underbrace{\left(\xi\frac{\partial w}{\partial x}+\eta\frac{\partial w}{\partial y}\right)}_{\text{B}} - \underbrace{\left(\frac{\partial \alpha}{\partial x}\frac{\partial p}{\partial y}-\frac{\partial \alpha}{\partial y}\frac{\partial p}{\partial x}\right)}_{\text{C}} + \underbrace{\left(\frac{\partial F_y}{\partial x}-\frac{\partial F_x}{\partial y}\right)}_{\text{D}}, \tag{5}$$

where $\boldsymbol{\omega}_h$ is the horizontal vorticity vector; ξ, η, and ζ are the x-, y-, and z-components of vorticity; u, v, and w are the x-, y-, and z-components of velocity; α is the specific volume of the air; p is the air pressure; and the vector $\boldsymbol{F}$ includes the diffusion and subgrid scale mixing (turbulence) terms.

Term A on the right in Eq. 3, Eq. 4 and Eq. 5 represents the stretching term while the term B represents the tilting term. These terms can be grouped together because both terms can stretch and tilt vortex lines (Davies-Jones 1982; Dahl et al. 2014). The pressure-volume solenoid term represents the baroclinic processes within the storm and is given by term C. Term D includes sub-grid scale (SGS) turbulence and implicit diffusion. These five terms described will be integrated to identify the mechanism to maintain the vortices. The individual terms of the vorticity budgets were retrieved via momentum forcing using the built-in diagnostics within CM1. Each of the momentum forcing terms was cross differentiated and the results were interpolated trilinearly to the locations of the parcels. Furthermore, the vorticity budget calculations were only applied to the parcels found according to the criteria discussed earlier. In addition, parcels that descended below the lowest scalar model level were excluded from the analysis following the recommendation by Vande Guchte and Dahl (2018).

Accepted for publication in *Monthly Weather Review*. DOI 10.1175/MWR-D-20-0082.1.

3. Results

a. Supercell

The supercell simulated for this study was located on the southern edge of a larger-scale QLCS (Fig. 2a). The supercell of interest forms from a right-moving split of the southernmost supercell at the start of the simulation. After the split, the storm begins to deviate from the larger-scale QLCS and begins to form a hook echo. Although the supercell remains fairly isolated, there is a downdraft in the forward flank (northeast of the updraft), which is possibly related to interactions with the other cells. The supercell then cycles and produces a second, more intense mesocyclone with the hook echo becoming more defined. The near-surface vertical vorticity fields show that a strong cyclonic vortex forms along the forward flank convergence boundary (FFCB, Beck and Weiss 2013) and strengthens into a persistent and more organized mesocyclone with the formation of the second hook echo. This second mesocyclone is the vortex that will be analyzed.

The parcel trajectories that met the criteria described in section 2b are shown in Fig. 2b with the representative trajectories used for the vorticity budgets drawn in purple. All of the 75 parcels that enter the mesocyclone are seen to originate within the forward flank outflow region of the supercell between 0.5 km and 3.5 km. There are two main mesocyclone entrance regions for the parcels, a northern and western region. Interestingly, all parcels appear to avoid entering the vorticity river (Dahl et al. 2014) seen along the FFCB northeast of the mesocyclone. The vertical cross-sections of Fig. 2b show that the parcels initially descend within the forward flank of the supercell and move towards the near-surface vortex prior to being lifted once they enter the low-level updraft.

The vorticity budgets calculated along the parcel trajectories provide insight into which of the forcing terms are most relevant in the vorticity evolution. The focus of this paper is on the near-

Accepted for publication in *Monthly Weather Review*. DOI 10.1175/MWR-D-20-0082.1.

surface vertical vorticity, but it is instructive to consider how the horizontal vorticity is acquired prior to being reoriented into the vertical.

A representative parcel was chosen from each of the entrance regions of the mesocyclone for a detailed analysis. These parcels both originate below 1 km and have likely made the majority of their decent prior to parcel initialization given their starting position (the average vertical vorticity of all parcels that remain of above the lowest model level will be shown later to discuss the representativeness of the chosen parcels). The western parcel comes from the north but eventually enters on the western edge of the mesocyclone. The vorticity budgets show reasonable agreement between the interpolated vorticity and the integrated vorticity for the magnitude of horizontal vorticity (ω_h) and vertical vorticity (ζ, Fig. 3a-d). The interpolated vorticity exhibits some noise, which we speculate is related to $2\Delta x$ waves. These are less visible in the smoother integrated forcing terms. Furthermore, once the parcels enter the vortex, the budgets become unreliable. In Fig. 3e-h, the individual time-integrated terms of the magnitude of horizontal vorticity and vertical vorticity of each trajectory are analyzed. The horizontal vorticity plots show that the stretching term is the primary driver of the magnitude of horizontal vorticity evolution (Fig. 3e,f). Consistent with this analysis, we see a lengthening of the wind vectors along the trajectories in Fig. 2b, which causes stretching of the horizontal vorticity and therefore increases the magnitude. The SGS terms also play an important role in modulating the horizontal vorticity. The significant magnitude of SGS could potentially be related to internal boundaries where there are large velocity gradients (Meneveau and Katz 2000). In both of these cases, the contributions to the horizontal vorticity from diffusion and baroclinity when compared to stretching and SGS are minimal. Importantly, the integrated terms of the vertical vorticity equation, shown in Fig. 3g,h, indicate that tilting and stretching of initially horizontal vorticity during vortex entrance are the main mechanisms by which large vertical vorticity arises. There is a noticable local minimum in vertical vorticity prior to the

Accepted for publication in *Monthly Weather Review*. DOI 10.1175/MWR-D-20-0082.1.

significant increase in the vertical vorticity around 7550 s (in Fig. 3g) and 7600 s (Fig. 3h). This dip is caused by numerical dispersion errors, causing stationary $2\Delta x$ waves (Durran 1999). These oscillations are also present in the simulation results by Dahl et al. (2014), Schenkman et al. (2014) and Markowski and Richardson (2014). The gradients resulting from the numerical dispersion lead to implicit diffusion, which leads to oscillations in the integrated budgets.

The main observation regarding the vorticity budget is that the large increase of vertical vorticity results from the rapid reorientation of horizontal vorticity close to the surface in rising air. The vertical vorticity thus only becomes significant after the parcel has passed the nadir, indicating that the DJB mechanism is not relevant for these parcels.

b. Quasi-two-dimensional Squall Line

All of the vortices that develop in this simulation form along the gust front ahead of the highest reflectivity values, as shown in Fig. 4. As expected, the vertical vorticity is not as strong as in the supercell simulation. The strongest updrafts have relatively large vertical vorticity ($\zeta = 0.05$ s^{-1}) for a few time steps, then weaken and strengthen again as a new updraft develops along the gust front. This process continues throughout the simulation.

Parcel trajectories for the squall line originate from the downdraft region of the storm and enter the vortex from the west within outflow air (Fig. 4), similar to the supercell case. The trajectories calculated within the squall line simulation are analyzed over a longer time period to be able to capture the initial descent of the parcels toward the surface. The 14 parcels that entered the mesovortex were initialized almost 3000 seconds (50 minutes) prior with a rather steep descent occurring early on and a more gradual descent to the surface thereafter (Fig. 4b).

The vorticity budget terms behave similarly to the supercell, but the magnitude of both the horizontal and vertical vorticity components is smaller (Fig. 5a,b). The horizontal vorticity budgets

Accepted for publication in *Monthly Weather Review*. DOI 10.1175/MWR-D-20-0082.1.

are largely affected by stretching and baroclinity (Fig. 5c). The smaller magnitude of stretching relative to the supercell case is related to the weaker horizontal accelerations in the squall line simulation. In contrast to the supercell case, the baroclinic term is a secondary forcing for horizontal vorticity, and becomes the primary forcing at the end of the time series. This is likely due to the earlier restart time resulting in longer parcel histories, which captures the baroclinic production during the early descent of the parcels, as well as a strong buoyancy gradient across the gust front (not shown). The SGS term is much smaller because of less turbulent motion and smaller velocity gradients in the squall line than in the supercell (Fig. 5c).

The time-integrated vertical vorticity terms show significant similarities to the supercell. Tilting and stretching continues to drive the vertical vorticity amplification with smaller contributions from the other time-integrated terms (Fig. 5d). Similarly to the supercell, as the parcel approaches its nadir, the vertical vorticity is near zero, implying that the DJB mechanism is practically absent because the vertical vorticity is decreasing as it approaches the nadir. Also, the local maxima and minima of vertical vorticity prior to reaching the nadir between 4500 and 5500 s are likely due to the series of weak updrafts and downdrafts seen by the parcel's height in Fig. 5b. At this point, the parcel is not within the lowest 100 m AGL and the vertical vorticity is not associated with the vortex of interest. This indicates that the reorientation of horizontal vorticity into vertical vorticity is occurring after the parcel reaches the updraft associated with the vortex. Also, the implicit diffusion dip and peak are seen again in the squall line simulation just prior to the significant increase in vertical vorticity as the parcel enters the vortex (Fig. 5d).

c. QLCS

At the beginning of the QLCS simulation, three updrafts develop and then split. Due to the storm splitting, interactions between the storms occur and the system begins to grow upscale into

Accepted for publication in *Monthly Weather Review*. DOI 10.1175/MWR-D-20-0082.1.

a QLCS (Fig. 6), while the supercell described in Section 3a deviates to the south. Consistent with previous research, our simulated QLCS develops a majority of its mesovortices north of the apex of the system (Weisman and Trapp 2003).

A segment along the northern half of the QLCS was considered, as it produces two strong and persistent vortices (Fig. 6). The trajectories for the QLCS are consistent with the results found in the supercell and squall line simulations (Fig. 6b). All of the 61 parcels that enter the specified window originate within the outflow of the QLCS. The parcels have a long time history and are initialized 1800 seconds (30 minutes) prior to entering the mesovortex. Early in the analysis period, the parcels begin to rapidly descend towards the surface. The parcels then move along the surface and gradually reach their nadirs before entering one of the two mesovortices (Fig. 6b, Fig. 7c,d).

As was the case with the trajectories in both the supercell and squall line simulations, the stretching term continues to be a significant forcing term in the horizontal vorticity budgets due to stretching caused by the acceleration of the wind (Fig. 6, Fig. 7e,f). The SGS term is as significant as the stretching term at some points along the trajectory of the horizontal vorticity. The vertical vorticity reaches significant values near the surface only after reaching the updraft with the tilting and stretching term providing the main forcing for the increase of vertical vorticity (Fig. 7g,h). In fact, the vertical vorticity in both QLCS mesovortices is negative prior to becoming positive as the parcel enters the mesovortex. The negative values of vertical vorticity indicate that the DJB mechanism is not present in the representative trajectories since they are not acquiring cyclonic vertical vorticity during their descent.

4. Discussion

Through the analysis of the trajectories and vorticity budgets, we find that the near-surface vertical vorticity, following the parcel motion, develops through the reorientation of horizontal

Accepted for publication in *Monthly Weather Review*. DOI 10.1175/MWR-D-20-0082.1.

vorticity into the vertical at the base of the vortex. To check whether the selected trajectories are representative of the bulk behavior, we show the averaged parcel in Fig. 8. Especially close to the vortex, the interpolated vertical vorticity of the representative trajectories align reasonably well with the average interpolated vertical vorticity of the remaining trajectories. The time has been normalized, such that every parcel enters the vortex at t = 0. We therefore feel confident that the mechanism captured by the individual trajectories is reasonably representative of the airflow into the vortices. The diverse results found in previous studies are, at least in part, likely tied to the different altitudes in which the vortices were analyzed. In simulating the multiple storm modes and keeping the altitude consistent across the three simulations, our study found one common mechanism across all storm modes within in the lowest 100 meters, i.e., the vorticity is tilted in the rising air described by Rotunno et al. (2017).

These results seem at odds with a large body of research (e.g., Davies-Jones 1982; Davies-Jones and Brooks 1993; Dahl et al. 2014; Markowski and Richardson 2014; Parker and Dahl 2015) that demonstrated that vertical vorticity at the surface must develop within a downdraft. We hypothesize that this discrepancy is tied to the maturity of the vortex. The initial emergence of vertical vorticity seems to require the DJB mechanism, but once a sufficient pressure deficit develops in the vortex core (Dahl 2020), the horizontal vorticity may be tilted into the vertical practically at the ground[2]. This hypothesis is being explored in ongoing work to quantify what defines a sufficient pressure deficit. Indeed, pressure deficits have developed in all of the vortices analyzed herein (Fig. 9).

An interesting aspect is that the parcels either do not pass through vertical-vorticity rivers (e.g., in the supercell simulation), or the absence of rivers altogether (e.g., the 2D squall line simulation, Fig. 10). In light of the absence of the DJB mechanism, this is perhaps not surprising, because the

[2]In real-world vortices, the horizontal vorticity may be scooped up practically at the surface within the corner-flow region (Lewellen and Lewellen 2007); in our simulations, this process cannot be resolved.

Accepted for publication in *Monthly Weather Review*. DOI 10.1175/MWR-D-20-0082.1.

parcels do not acquire vertical vorticity until they enter the vortex. It thus seems that the existence of vertical vorticity rivers is not required to maintain the vortices. The need for river-like vortex patches in vortex *genesis* is discussed by Dahl (2020).

The simulations performed in this study were free-slip. However, if surface friction was included, the fundamental results of acquiring near-surface vertical vorticity would likely not change. In fact, the "in-and-up" mechanism identified in this work would likely be enhanced because the vortex structure would be more realistic, allowing for more abrupt upward tilting and a frictional enhancement of near-surface horizontal vorticity; see Schenkman et al. (2012), Roberts et al. (2016), Roberts and Xue (2017).

Despite the variety of processes that have been proposed to maintain vortices in supercells and QLCSs, we find that mature vortices only require the presence of a near-surface updraft and pressure deficit to first stretch horizontal vorticity, which may then be tilted upward abruptly (Fig. 9, Fig. 11). Considering the results, it seems possible that ultimately tornado-like vortices may be driven by the same basic mechanism across different storm structures,[3] which also suggests that the nomenclature for near-surface vortices accompanying different storm structures may not be justified from a dynamical standpoint (e.g., near-surface mesovortex in QLCSs vs. near-surface mesocyclone in supercells).

5. Summary

The primary goal of this research was to identify the mechanism of maintaining large near-surface vertical vorticity across various storm modes including a supercell, a quasi-2D squall line, and a QLCS. To investigate the most relevant mechanism of acquiring near-surface vertical vorticity, idealized, free-slip, double-moment microphysics simulations were performed using CM1

[3]Maxworthy (1973) inferred the same mechanism for (mature) dust devils.

Accepted for publication in *Monthly Weather Review*. DOI 10.1175/MWR-D-20-0082.1.

to simulate the different storm modes at 200 m horizontal grid spacing. The simulations included long-history parcel trajectory and vorticity budget analyses. The parcels were only considered if they had acquired vertical vorticity of 0.01 s^{-1} within the vortex in the lowest 100 m AGL of the model domain.

The analysis in this study was performed on mature vortices yielding the following conclusions:

- The near-surface vertical vorticity (lowest 100 m AGL) is acquired as horizontal vorticity is tilted into the vertical and simultaneously stretched at the base of the vortex across all of the simulated storm modes (supercell, quasi-2D squall line, and QLCS). The parcels only achieve appreciable values of positive near-surface vertical vorticity after reaching their nadirs (and thus reaching the updraft). This indicates that the mechanism of upward vortex line tilting via the updraft is the most relevant mechanism in the maintenance of mature vortices analyzed herein.

- The Davies-Jones and Brooks (1993) mechanism (upward vortex line tilting via the downdraft) and the Trapp and Weisman (2003) mechanism (downward vortex line tilting via the downdraft) were not present in the parcel analysis within any of our simulations. However, we hypothesize that the initial emergence of vertical vorticity is still due to the DJB mechanism, and once a sufficiently strong pressure deficit vortex is present, the "in and up" mechanism becomes relevant.

- Across all storm modes simulated, the parcels entering the vortex originated within the outflow region of the storm.

- Parcels entering the vortex did not spend time in vertical vorticity rivers, or vertical vorticity rivers were entirely absent, consistent with the "in-and-up" mechanism identified herein.

Accepted for publication in *Monthly Weather Review*. DOI 10.1175/MWR-D-20-0082.1.

Further research is required to assess and further understand the "in and up" process for the maintenance of mature vortices, including what qualifies as a sufficient pressure deficit beyond which the DJB mechanism no longer seems to be required.

Data availability statement. The data acquired for this study was created using the Cloud Model 1 (CM1) developed by George Bryan at the National Center for Atmospheric Research. The source code for CM1 can be accessed at the following link: https://www2.mmm.ucar.edu/people/bryan/cm1/.

Acknowledgments. The authors wish to thank Dr. George Bryan for providing and maintaining the CM1 source code as well as Drs. Paul Markowski and Matt Parker for numerous beneficial discussions. We also thank Matt Flournoy and two anonymous reviewers for their thoughtful comments that helped clarify and improve the presentation of the manuscript. We also thank the first author's committee members, Drs. Brian Ancell and Eric Bruning for helpful comments on improving the research in this study. We would also like to acknowledge the support of the High Performance Computing Center at Texas Tech University. Funding for Johannes M. L. Dahl came from the NSF grant AGS-1651786.

References

Atkins, N. T., and M. St. Laurent, 2009: Bow echo mesovortices. Part II: Their genesis. *Mon. Wea. Rev.*, **137**, 1514–1532, doi:10.1175/2008MWR2650.1.

Beck, J., and C. Weiss, 2013: An asessment of low-level baroclinity and vorticity within a simulated supercell. *Mon. Wea. Rev.*, **141**, 649–669, doi:10.1175/MWR-D-11-00115.1, URL http://journals.ametsoc.org/doi/abs/10.1175/MWR-D-11-00115.1.

Accepted for publication in *Monthly Weather Review*. DOI 10.1175/MWR-D-20-0082.1.

Bryan, G. H., and J. M. Fritsch, 2002: A benchmark simulation for moist nonhydrostatic numerical models. *Mon. Wea. Rev.*, **130**, 2917–2928, doi:https://doi.org/10.1175/1520-0493(2002)130<2917:ABSFMN>2.0.CO;2.

Dahl, J. M. L., 2015: Near-ground rotation in simulated supercells: On the robustness of the baroclinic mechanism. *Mon. Wea. Rev.*, **143**, 4929–4942, doi:10.1175/MWR-D-15-0115.1.

Dahl, J. M. L., 2020: Near surface vortex formation in supercells from the perspective of vortex patch dynamics. *Mon. Wea. Rev.*, submitted.

Dahl, J. M. L., M. D. Parker, and L. J. Wicker, 2014: Imported and storm-generated near-ground vertical vorticity in a simulated supercell. *J. Atmos. Sci.*, **71**, 3027–3051, doi:10.1175/JAS-D-13-0123.1, URL http://journals.ametsoc.org/doi/abs/10.1175/JAS-D-13-0123.1.

Davies-Jones, R., 1982: *Observational and theoretical aspects of tornadogenesis*. L. Bengtsson and J. Lighthill, Eds., Springer, 175–189 pp.

Davies-Jones, R., 2000: A Lagrangian model for baroclinic genesis of mesoscale vortices. Part I: Theory. *J. Atmos. Sci.*, **57**, 715–736, doi:10.1175/1520-0469(2000)057<0715:ALMFBG>2.0.CO;2.

Davies-Jones, R., 2017: Roles of streamwise and transverse partial-vorticity components in steady inviscid isentropic supercell-like flows. *J. Atmos. Sci.*, **74**, 3021–3041, doi:10.1175/JAS-D-16-0332.1.

Davies-Jones, R., and H. E. Brooks, 1993: Mesocyclone from a theoretical perspective. *American Geophysical Union*, 105–114.

Dawson, D. T., M. Xue, J. A. Milbrandt, and M. K. Yau, 2010: Comparison of evaporation and cold pool development between single-moment and multimoment bulk microphysics schemes

Accepted for publication in *Monthly Weather Review*. DOI 10.1175/MWR-D-20-0082.1.

in idealized simulations of tornadic thunderstorms. *Mon. Wea. Rev.*, **138**, 1152–1171, doi: 10.1175/2009MWR2956.1.

Durran, D. R., 1999: *Numerical methods for wave equations in geophysical fluid dynamics*. Springer Science & Business Media, 73 pp.

Flournoy, M. D., and M. C. Coniglio, 2019: Origins of vorticity in a simulated tornadic mesovortex observed during PECAN on 6 July 2015. *Mon. Wea. Rev.*, **147**, 107–134, doi:10.1175/MWR-D-18-0221.1, URL http://journals.ametsoc.org/doi/10.1175/MWR-D-18-0221.1.

Lewellen, D. C., and W. S. Lewellen, 2007: Near-surface intensification of tornado vortices. *J. Atmos. Sci.*, **64**, 2176–2194, doi:10.1175/JAS3965.1.

Markowski, P., Y. Richardson, E. Rasmussen, J. Straka, R. Davies-Jones, and R. J. Trapp, 2008: Vortex lines within low-level mesocyclones obtained from pseudo-dual-Doppler radar observations. *Mon. Wea. Rev.*, **136**, 3513–3535, doi:10.1175/2008MWR2315.1, URL http://journals.ametsoc.org/doi/abs/10.1175/2008MWR2315.1.

Markowski, P. M., and Y. Richardson, 2014: The influence of environmental low-level shear and cold pools on tornadogenesis: Insights from idealized simulations. *J. Atmos. Sci.*, **71**, 243–275, doi:10.1175/JAS-D-13-0159.1.

Mashiko, W., 2016: A numerical study of the 6 May 2012 Tsukuba city supercell tornado. Part I : Vorticity sources of low-level and midlevel mesocyclones. *Mon. Wea. Rev.*, **144**, 1069–1092, doi:10.1175/MWR-D-15-0123.1.

Maxworthy, T., 1973: A Vorticity Source for Large-Scale Dust Devils and Other Comments on Naturally Occurring Columnar Vortices. *J. Atmos. Sci.*, **30**, 1717–1722, doi: 10.1175/1520-0469(1973)030<1717:avsfls>2.0.co;2.

Accepted for publication in *Monthly Weather Review*. DOI 10.1175/MWR-D-20-0082.1.

Meneveau, C., and J. Katz, 2000: Scale-invariance and turbulence models for large-eddy simulations. *Annual Rev. Fluid Mech.*, **32**, 1–32.

Morrison, H., J. A. Curry, and V. Khvorostyanov, 2005: A new double-moment microphysics parameterization for application in cloud and climate models. Part I : Description. *J. Atmos. Sci.*, **62**, 1665–1677.

Parker, M. D., 2012: Impacts of lapse rates on low-level rotation in idealized storms. *J. Atmos. Sci.*, **69**, 538–559, doi:10.1175/JAS-D-11-058.1.

Parker, M. D., and J. M. L. Dahl, 2015: Production of near-surface vertical vorticity by idealized downdrafts. *Mon. Wea. Rev.*, **143**, 2795–2816, doi:10.1175/MWR-D-14-00310.1, URL http://journals.ametsoc.org/doi/abs/10.1175/MWR-D-14-00310.1.

Roberts, B., and M. Xue, 2017: The role of surface drag in mesocyclone intensification leading to ornadogenesis within an idealized supercell simulation. *J. Atmos. Sci.*, **74**, 3055–3077, doi:10.1175/JAS-D-16-0364.1.

Roberts, B., M. Xue, and D. T. Dawson, 2020: The Effect of Surface Drag Strength on Mesocyclone Intensification and Tornadogenesis in Idealized Supercell Simulations. *J. Atmos. Sci.*, **77**, 1699–1721, doi:10.1175/jas-d-19-0109.1.

Roberts, B., M. Xue, A. D. Schenkman, and D. T. Dawson, 2016: The role of surface drag in tornadogenesis within an idealized supercell simulation. *J. Atmos. Sci.*, **73**, 3371–3395, doi:10.1175/JAS-D-15-0332.1.

Rotunno, R., J. B. Klemp, and M. L. Weisman, 1988: A theory for strong, long-lived squall lines. *J. Atmos. Sci.*, **45**, 463–485, doi:https://doi.org/10.1175/1520-0469(1988)045<0463:ATFSLL>2.0.CO;2.

Accepted for publication in *Monthly Weather Review*. DOI 10.1175/MWR-D-20-0082.1.

Rotunno, R., P. M. Markowski, and G. H. Bryan, 2017: " Near ground " vertical vorticity in supercell thunderstorm models. *J. Atmos. Sci.*, **74**, 1757–1766, doi:10.1175/JAS-D-16-0288.1.

Schenkman, A. D., M. Xue, and M. Hu, 2014: Tornadogenesis in a high-resolution simulation of the 8 May 2003 Oklahoma City supercell. *J. Atmos. Sci.*, **71**, 130–154, doi:10.1175/JAS-D-13-073.1.

Schenkman, A. D., M. Xue, and A. Shapiro, 2012: Tornadogenesis in a simulated mesovortex within a mesoscale convective system. *J. Atmos. Sci.*, **69**, 3372–3390, doi:10.1175/JAS-D-12-038.1.

Trapp, R. J., and M. L. Weisman, 2003: Low-level mesovortices within squall lines and bow echoes. Part II: Their genesis and implications. *Mon. Wea. Rev.*, **131**, 2804–2823, doi:10.1175/1520-0493(2003)131<2804:LMWSLA>2.0.CO;2.

Vande Guchte, A., and J. M. L. Dahl, 2018: Sensitivities of parcel trajectories beneath the lowest scalar model level of a Lorenz vertical grid. *Mon. Wea. Rev.*, **146**, 1427–1435, doi:10.1175/MWR-D-17-0190.1.

Weisman, M. L., and R. J. Trapp, 2003: Low-level mesovortices within squall lines and bow echoes. Part I: Overview and dependence on environmental shear. *Mon. Wea. Rev.*, **131**, 2779–2803, doi:https://doi.org/10.1175/1520-0493(2003)131<2779:LMWSLA>2.0.CO;2.

Accepted for publication in *Monthly Weather Review*. DOI 10.1175/MWR-D-20-0082.1.

LIST OF FIGURES

Accepted for publication in *Monthly Weather Review*. DOI 10.1175/MWR-D-20-0082.1.

Accepted for publication in *Monthly Weather Review*. DOI 10.1175/MWR-D-20-0082.1.

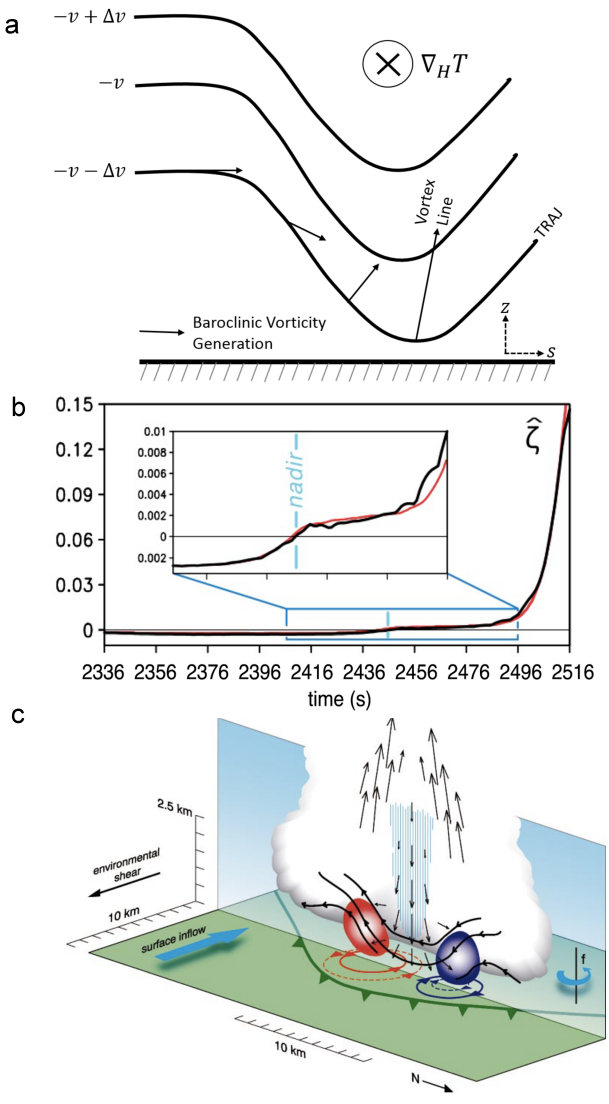

480 FIG. 1. The Davies-Jones and Brooks (1993) mechanism is presented in a), where the vorticity vector attains
481 an upward inclination during descent. The Rotunno et al. (2017) mechanism is represented in b), where the
482 updraft tilts the horizontal vorticity with the interpolated vertical vorticity (black), the integrated vertical vorticity
483 (red) and the nadir (cyan) with a zoomed-in region within the subset. Finally, the Trapp and Weisman (2003)
484 mechanism is shown in c), where the downdrafts tilts the horizontal vorticity downward; shown are the vortex
485 lines (bold black), positive vertical vorticity (red), negative surface vertical vorticity (purple), the gust front
486 (green) and the air motion (black vectors).

Accepted for publication in *Monthly Weather Review*. DOI 10.1175/MWR-D-20-0082.1.

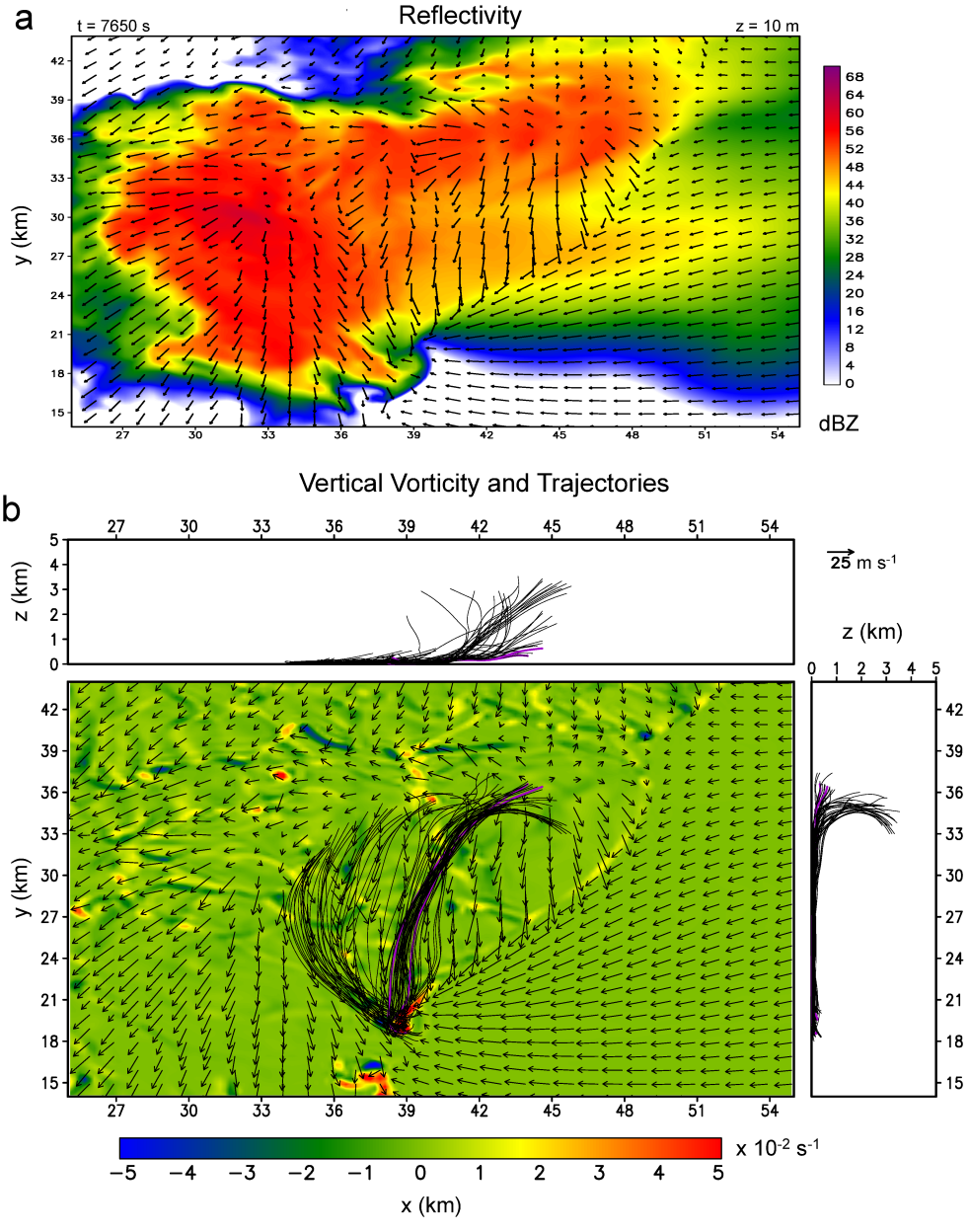

487 FIG. 2. (a) Reflectivity (shaded) and (b) vertical vorticity (shaded) with the horizontal velocity vectors of the
488 supercell simulation at 7650 s at the lowest model level (10 m AGL). The parcel trajectories (black, solid lines)
489 are included in panel b) with the trajectories used for the vorticity budget calculations highlighted in purple.

Accepted for publication in *Monthly Weather Review*. DOI 10.1175/MWR-D-20-0082.1.

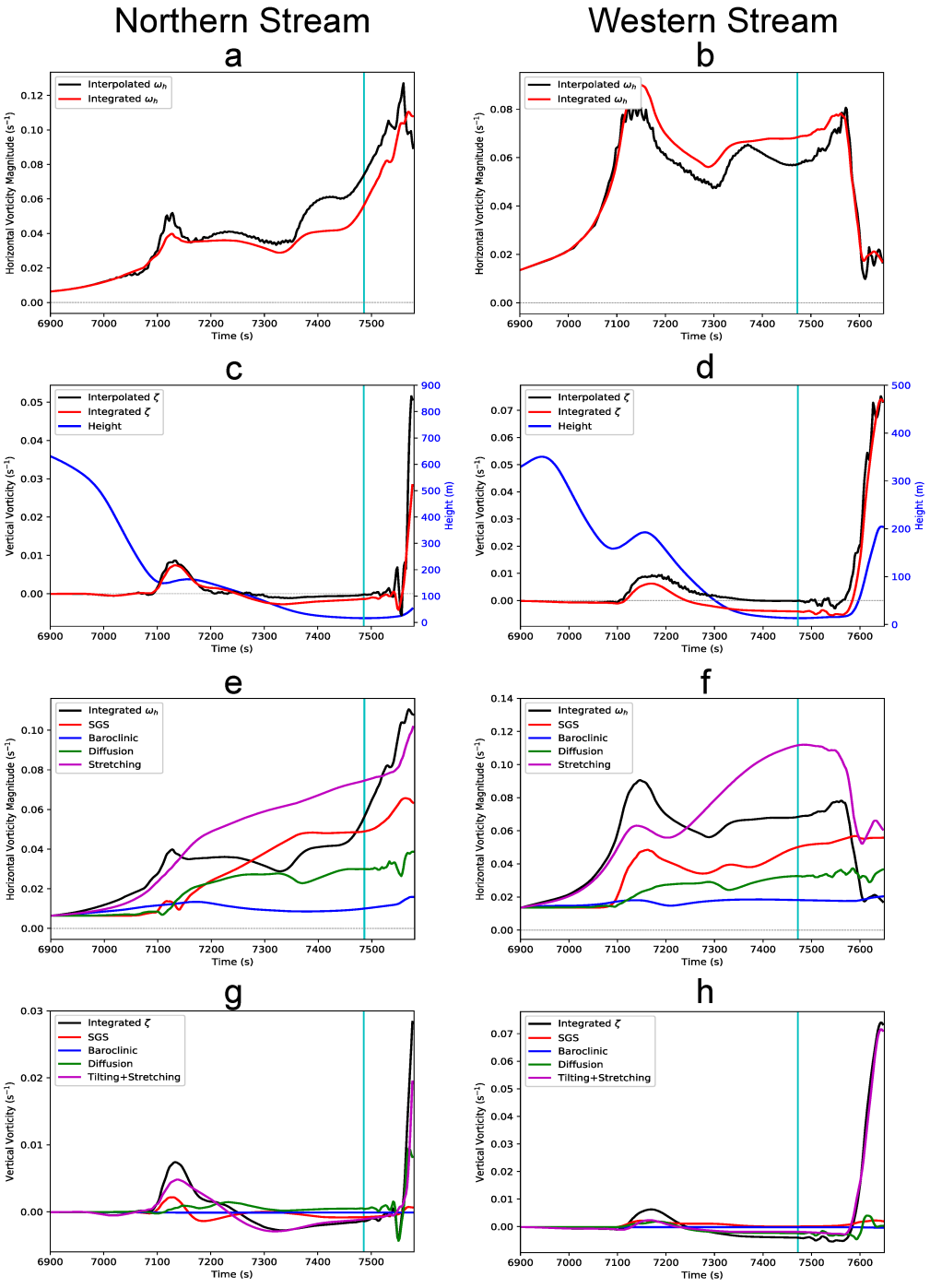

490 FIG. 3. Shown are the vorticity evolution for the western stream (left column) and northern stream (right
491 column) of the supercell parcels. (a,b): Interpolated horizontal vorticity (black) and integrated horizontal
492 vorticity (red); (c,d) interpolated vertical vorticity (black) and integrated vertical vorticity (red). Parcel height is
493 shown in blue. (e,f): Integrated forcing terms of the horizontal vorticity, color-coded according to the legend.
494 (g,h): Integrated forcing terms of the vertical vorticity, color-coded according to the legend.

Accepted for publication in *Monthly Weather Review*. DOI 10.1175/MWR-D-20-0082.1.

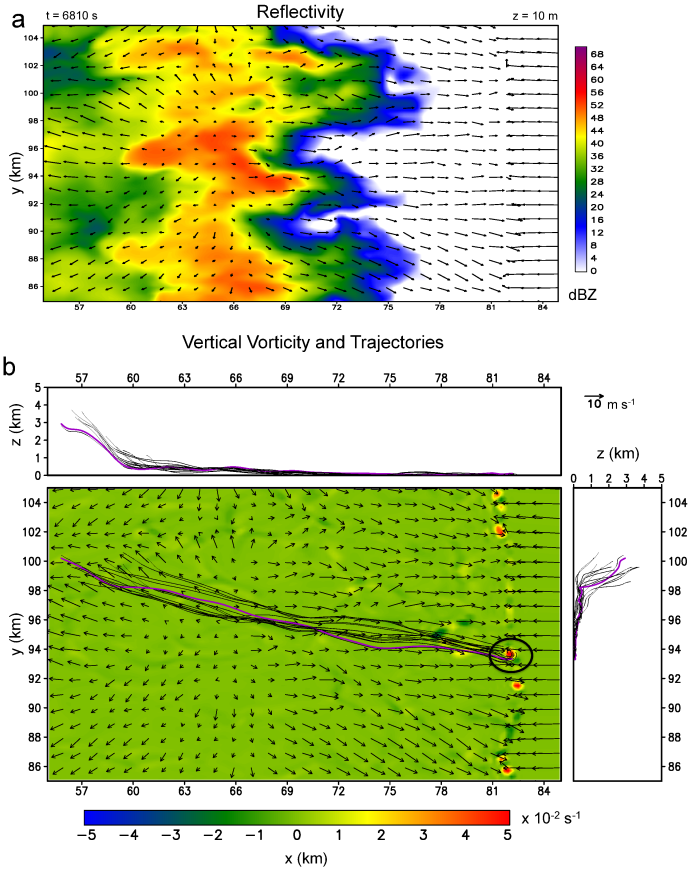

FIG. 4. As in Fig. 2 but for the squall line simulation at 6810 s. The vortex used for analysis is circled in b).

Accepted for publication in *Monthly Weather Review*. DOI 10.1175/MWR-D-20-0082.1.

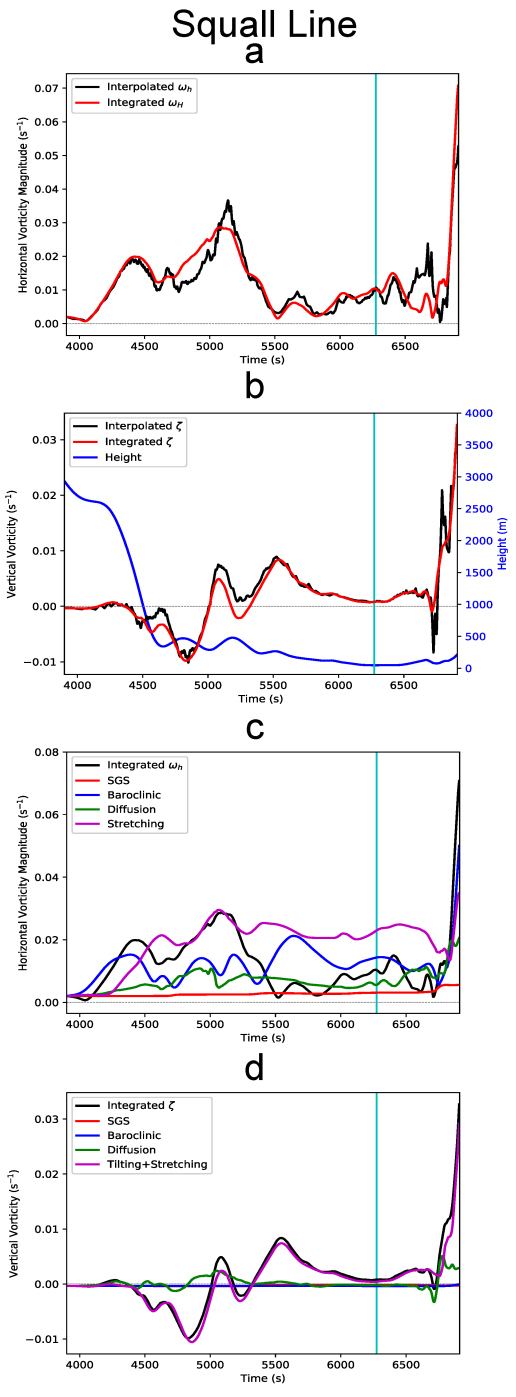

FIG. 5. Shown is the vorticity evolution for the squall line parcels. (a): Interpolated horizontal vorticity (black) and integrated horizontal vorticity (red); (b) interpolated vertical vorticity (black) and integrated vertical vorticity (red). Parcel height is shown in blue. (c): Integrated forcing terms of the horizontal vorticity, color-coded according to the legend. (d): Integrated forcing terms of the vertical vorticity, color-coded according to the legend.

Accepted for publication in *Monthly Weather Review*. DOI 10.1175/MWR-D-20-0082.1.

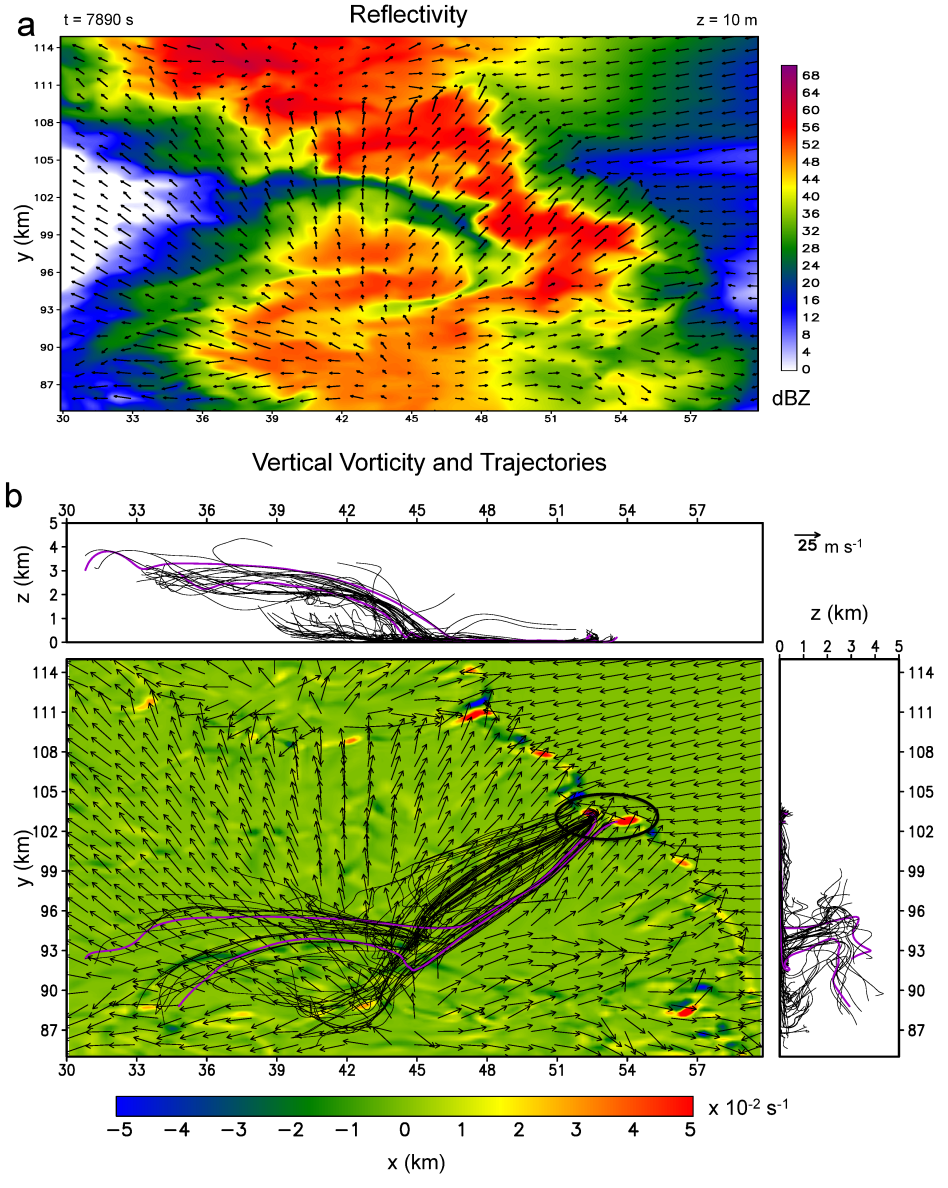

FIG. 6. As in Fig. 2 but for the QLCS simulation at 7890 s. The vortices used for analysis is circled in b.

Accepted for publication in *Monthly Weather Review*. DOI 10.1175/MWR-D-20-0082.1.

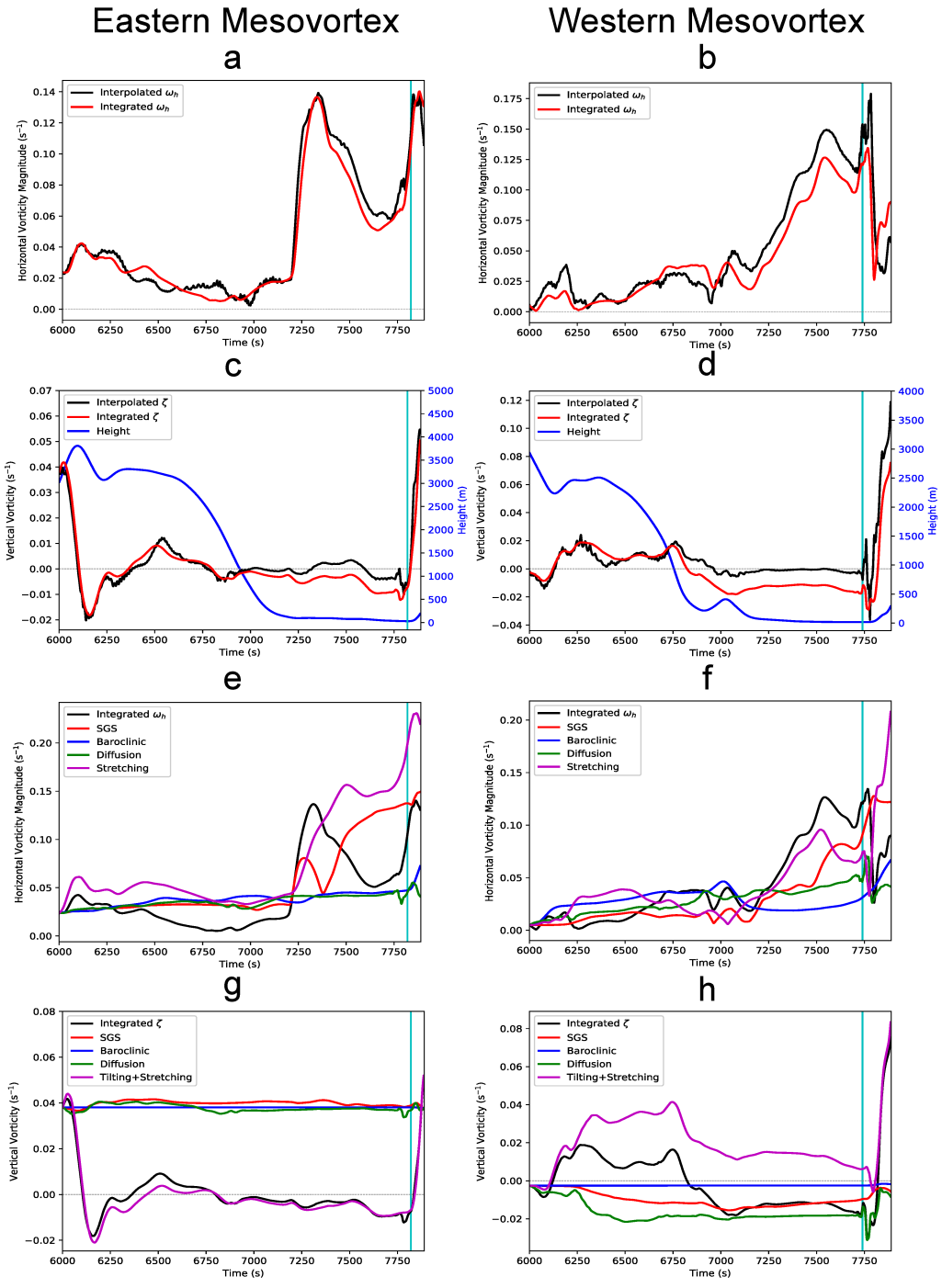

500 FIG. 7. As in Fig. 3 but for the QLCS simulation with the eastern mesovortex (left) and the western mesovortex
501 (right).

Accepted for publication in *Monthly Weather Review*. DOI 10.1175/MWR-D-20-0082.1.

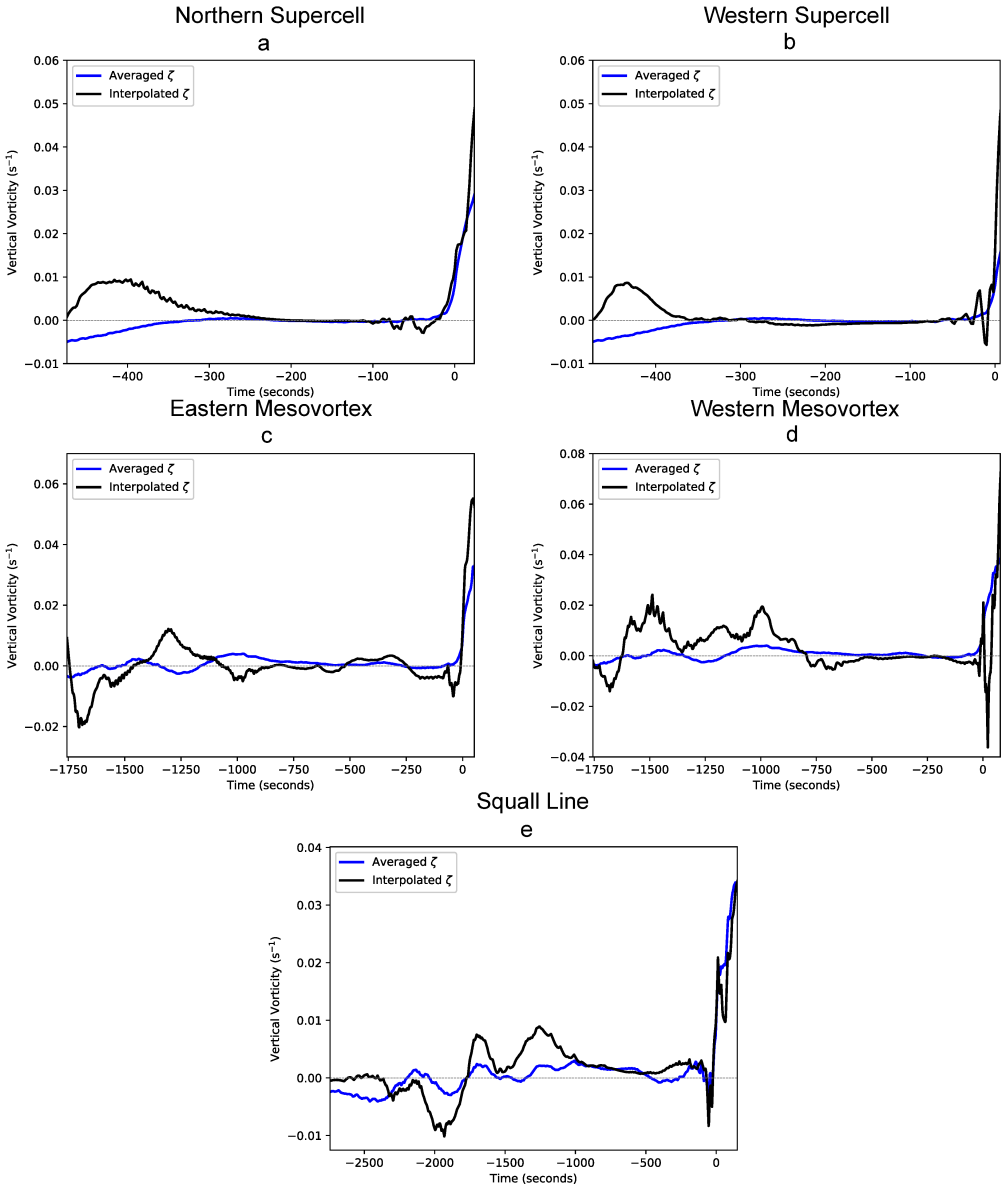

502 FIG. 8. The average vertical vorticity of all trajectories above the lowest model level (blue) against the
503 interpolated vertical vorticity (black) of each representative trajectory used for the vorticity budgets for (a,b)
504 supercell, (c,d) QLCS, and (e) squall line.

Accepted for publication in *Monthly Weather Review*. DOI 10.1175/MWR-D-20-0082.1.

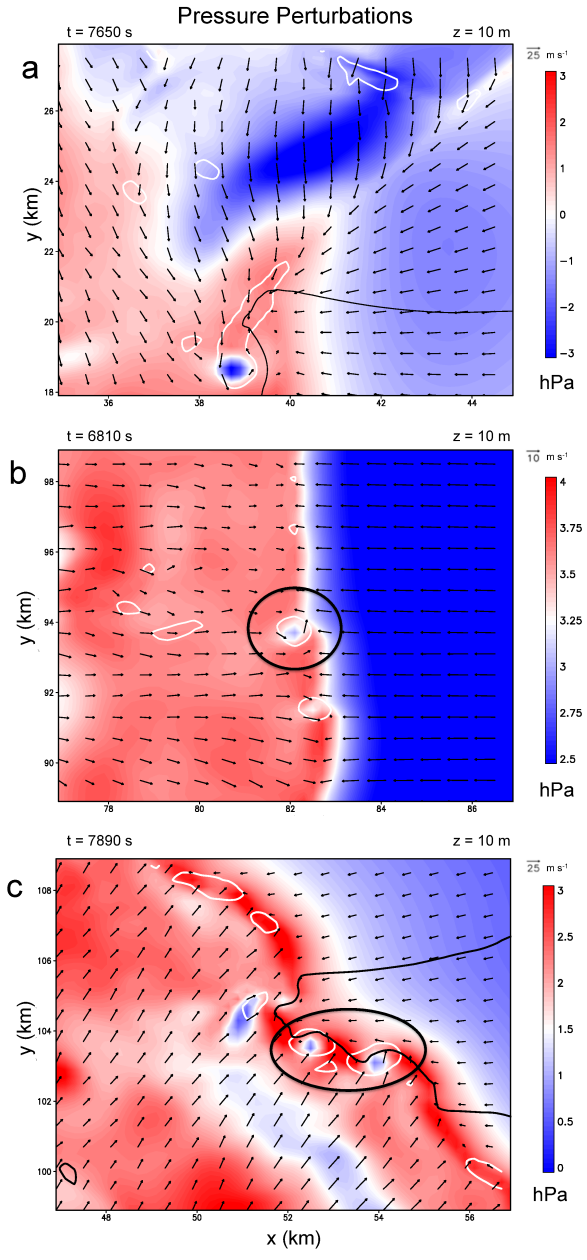

FIG. 9. The pressure perturbations (shaded) with the 0.01 s^{-1} vertical vorticity (contoured, white) and the horizontal velocity vectors for a) the supercell at 7650 s, b) the squall line at 6810 s and c) the QLCS at 7890 s at the lowest model level. The analyzed vortices are circled in b) and c). Note the different scale of the colorbars.

Accepted for publication in *Monthly Weather Review*. DOI 10.1175/MWR-D-20-0082.1.

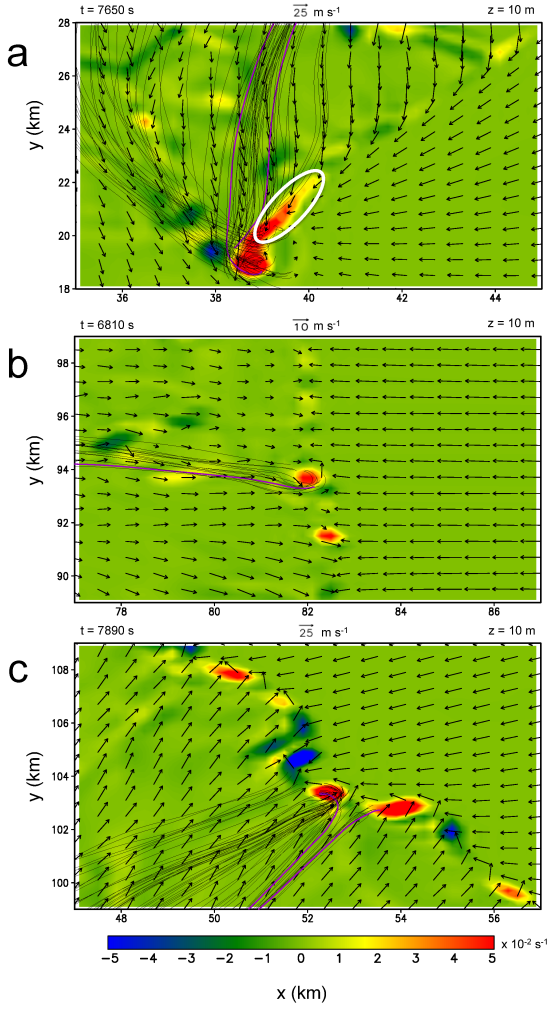

508 FIG. 10. Vertical vorticity (shaded) and trajectories zoomed in for view of vortices of the (a) supercell, (b)
509 squall line and (c) QLCS. The vertical vorticity river is encircled in a).

Accepted for publication in *Monthly Weather Review*. DOI 10.1175/MWR-D-20-0082.1.

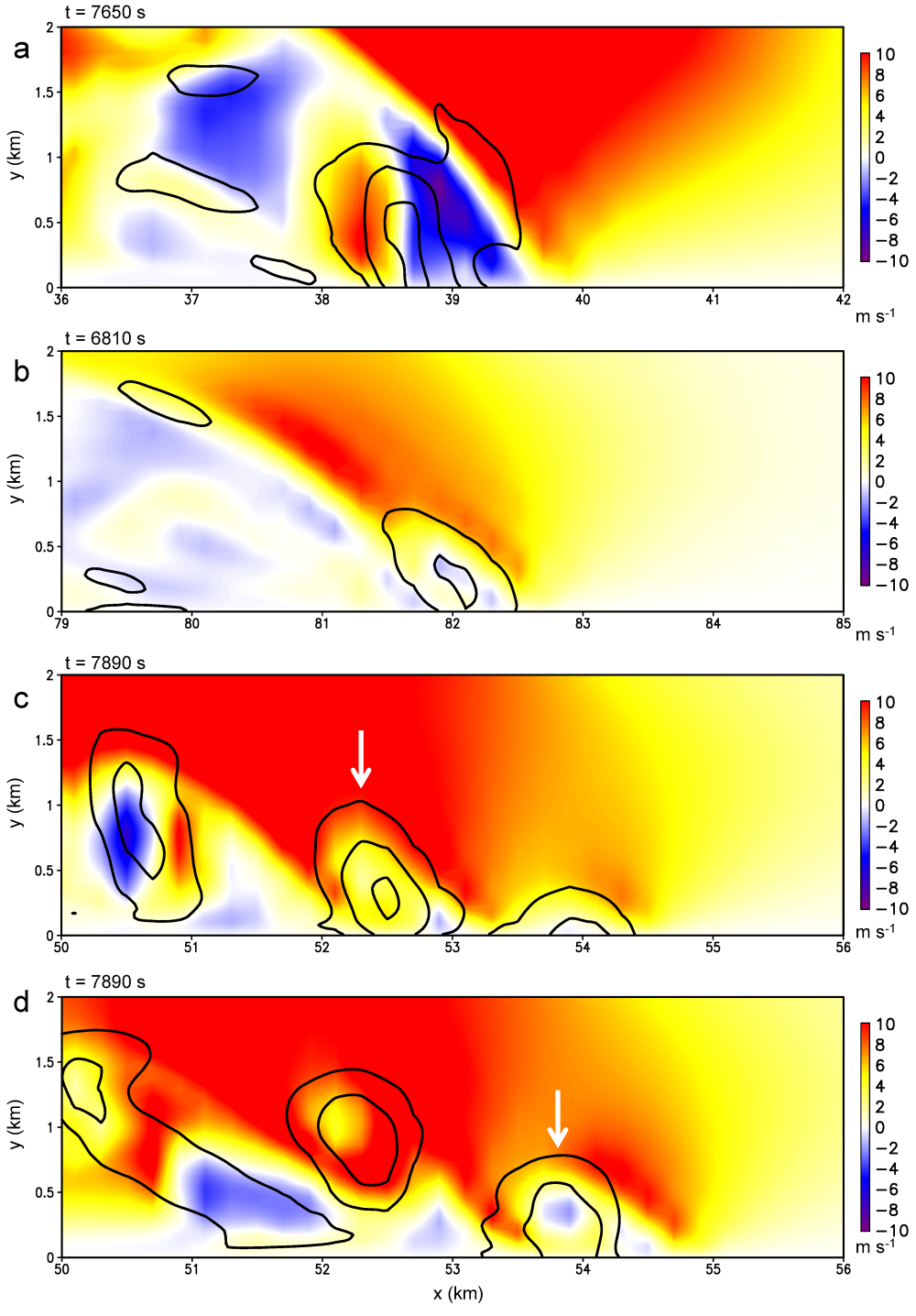

FIG. 11. A vertical cross-section of vertical velocity (shaded) and vertical vorticity (contoured at 0.01 s^{-1}, 0.05 s^{-1} and 0.1 s^{-1}) across the updraft of the individual vortices for the (a) supercell at y = 18.4 km and 7650 s, (b) squall line at y = 93.6 km and 6810 s, (c) the QLCS western mesovortex at y = 103.6 km and 7890 s and (d) the QLCS eastern mesovortex at y = 103.2 km and 7890 s. The vortices discussed in the text are indicated by the arrow in c) and d).

Accepted for publication in *Monthly Weather Review*. DOI 10.1175/MWR-D-20-0082.1.